Article

Topological water-wave structures manipulating particles

https://doi.org/10.1038/s41586-024-08384-y

Received: 14 May 2024

Accepted: 11 November 2024

Published online: 5 February 2025

Check for updates

Bo Wang[1,2,3,11], Zhiyuan Che[1,4,11], Cheng Cheng[1,4], Caili Tong[2], Lei Shi[1,4]✉, Yijie Shen[5,6,7]✉, Konstantin Y. Bliokh[8,9,10]✉ & Jian Zi[1,4]✉

Topological wave structures, such as vortices[1–6], polarization textures[7–11] and skyrmions[12–19], appear in various quantum and classical wave fields, including optics and acoustics. In particular, optical vortices have found numerous applications[20,21], ranging from quantum information to astrophysics. Furthermore, both optical and acoustic structured waves are crucial in the manipulation of small particles[22–25], from atoms to macroscopic biological objects. Recently, there has been a surge of interest in structured water surface waves, which can be notable analogues of quantum, optical and acoustic wave systems[26–29]. However, topological water-wave forms, especially their ability to manipulate particles, have not yet been demonstrated. Here we describe the controllable generation of topological structures, namely wave vortices, skyrmions and polarization Möbius strips, in gravity water waves. Most importantly, we demonstrate the efficient manipulation of subwavelength and wavelength-order floating particles with topologically structured water waves. This includes trapping the particles in the high-intensity field zones and controlling their orbital and spinning motion due to the orbital and spin angular momenta of the water waves. Our results reveal the water-wave counterpart of optical and acoustic manipulation, which paves the way for applications in hydrodynamics and microfluidics.

Linear plane waves, which are sinusoidal oscillations propagating in one direction, are characterized by a few key parameters: amplitude, phase, frequency, wavevector and polarization. These are equally relevant for acoustic, electromagnetic, quantum and hydrodynamical waves. However, when several plane waves interfere, the resulting structured field becomes rather complicated, so that its amplitude, phase and polarization can vary arbitrarily from point to point[30,31]. For such complex wave fields, topological properties, robust with respect to small perturbations, become relevant.

Topological wave forms, such as phase singularities (wave vortices)[1–6], polarization singularities and Möbius strips[3,7–11], as well as skyrmions and merons[11–19], play important roles in various areas of modern wave physics. In addition to the topological robustness, these structures exhibit notable dynamical properties. For example, wave vortices carry quantum-mechanical-like orbital angular momentum (OAM)[4,6,20,21]. That is why vortex and, generally, structured waves have enormously advanced the optical and acoustic manipulation of small particles[22–25].

Surface water waves are the most accessible classical waves[32]. Surprisingly, systematic studies of linear structured water waves with non-trivial topological and dynamical properties, which resemble optical and acoustic structured waves, began only recently[26–29,33–36]. Water-wave vortices with different topological charges, skyrmions and polarization Möbius strips have been described theoretically[37,38].

In this work, we present the controllable generation of these topological structures in gravity water waves. We deal with two basic configurations. First, a suitable interference of three plane waves produces a lattice of (1) first-order vortices in the surface-elevation (vertical displacement) field, (2) skyrmions in the instantaneous three-dimensional surface-displacement field and (3) C-points of pure-circular 'polarizations' (three-dimensional trajectories of water-surface particles) surrounded by the polarization Möbius strips. Second, several circularly distributed, interfering waves with an azimuthal phase increment produce Bessel-type wave vortices with controllable topological charges. Most importantly, we demonstrate the efficient manipulation of macroscopic floating particles using structured water waves. In complete analogy with optical and acoustic forces and torques, we observe (1) the gradient force trapping particles in the high-wave-intensity areas, (2) the 'radiation-pressure' force pushing a particle along the local phase gradient (the wave momentum density) and (3) the torque on the particle produced by the effective spin density in the water-wave field.

Our results provide an efficient toolbox for manipulating floating objects with water waves and offer an accessible platform for studying the topological and dynamical properties of structured waves.

[1]State Key Laboratory of Surface Physics, Department of Physics, Fudan University, Shanghai, China. [2]Henan Key Laboratory of Quantum Materials and Quantum Energy, School of Quantum Information Future Technology, Henan University, Zhengzhou, China. [3]Institute of Quantum Materials and Physics, Henan Academy of Sciences, Zhengzhou, China. [4]Key Laboratory of Micro- and Nano-Photonic Structures (Ministry of Education), Fudan University, Shanghai, China. [5]Centre for Disruptive Photonic Technologies, School of Physical and Mathematical Sciences, Nanyang Technological University, Singapore, Singapore. [6]School of Electrical and Electronic Engineering, Nanyang Technological University, Singapore, Singapore. [7]International Institute for Sustainability with Knotted Chiral Meta Matter (WPI-SKCM2), Hiroshima University, Hiroshima, Japan. [8]Donostia International Physics Center (DIPC), Donostia-San Sebastián, Spain. [9]Theoretical Quantum Physics Laboratory, Cluster for Pioneering Research, RIKEN, Saitama, Japan. [10]Centre of Excellence ENSEMBLE3, Warsaw, Poland. [11]These authors contributed equally: Bo Wang, Zhiyuan Che. ✉e-mail: lshi@fudan.edu.cn; yijie.shen@ntu.edu.sg; konstantin.bliokh@dipc.org; jzi@fudan.edu.cn

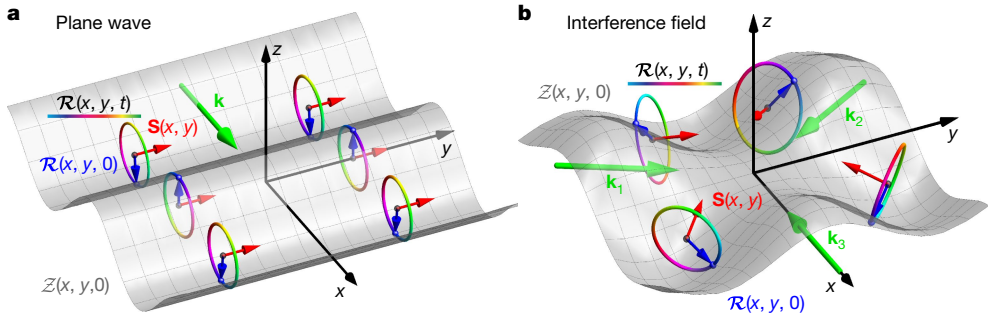

Fig. 1 | Linear water waves and their main local characteristics. **a**,**b**, Wavevectors **k** (green), the wave-perturbed water surface $z = \mathcal{Z}(x, y, t = 0)$ (grey), the local three-dimensional displacement of the water-surface particles $\mathcal{R}(x, y, 0)$ (blue), the local elliptical trajectories (polarizations) of the water-surface particles traced by $\mathcal{R}(x, y, t)$ (rainbow colours indicate the periodic evolution in t) and the corresponding time-averaged spin angular-momentum density $\mathbf{S}(x,y)$ (red). **a**, A single plane wave propagating along the x axis. **b**, Interference of several plane waves with the same frequencies and amplitudes but with wavevectors in different directions.

Basic concepts

The main concepts applied in this work are shown in Fig. 1. We consider linear deep-water gravity water waves, but all the main results remain valid for gravity-capillary finite-depth water waves[32,38]. In the linear approximation, the water-surface particles, distributed over the two-dimensional $z = 0$ plane, oscillate in space and time, which can be characterized by the three-dimensional displacement of each particle with respect to its unperturbed position, $\mathcal{R}(x, y, t)$. The z component of this displacement, $\mathcal{Z}(x, y, t)$, describes the directly observable perturbed water surface.

Consider first a plane water wave with frequency ω and wavevector $\mathbf{k} = k\overline{\mathbf{x}}$ (the overbar denotes the unit vector of the corresponding direction), related as $\omega^2 = gk$, where g is the gravitational acceleration (Fig. 1a). In such a wave, the water-surface particles move along circular trajectories traced by $\mathcal{R}(x, y, t)$ in the (z,x) plane[32]. These circular trajectories and the corresponding local angular momentum produced by circling particles can be considered as fluid-mechanical analogues of circular polarization and spin angular-momentum density in electromagnetic or acoustic waves[28,38–41].

In a plane water wave, the circular polarization and the corresponding spin vectors are similar for all water-surface particles. However, when we interfere several plane water waves with the same frequency but different wavevectors, the behaviour of particles in different points of the (x,y) plane varies dramatically (Fig. 1b). The trajectory of each particle is now a generic ellipse in three-dimensional space, with the corresponding spin normal to its plane. Such a structured wave field is conveniently described by the complex displacement field $\mathbf{R}(x,y)$: $\mathcal{R}(x, y, t) = \mathrm{Re}[\mathbf{R}(x, y)e^{-i\omega t}]$. The corresponding spin density is $\mathbf{S} = (\rho\omega/2)\mathrm{Im}(\mathbf{R}^* \times \mathbf{R})$, where ρ is the water density[28,38]. Below we study topological structures in gravity water waves using the vector surface-displacement field $\mathcal{R}$ or $\mathbf{R}$, and its physically meaningful quadratic forms, such as the spin density $\mathbf{S}$.

Vortices, skyrmions and Möbius strips

Our experiments were performed in a square 60×60 cm^2 wave tank with a depth $h = 3$ cm. We used wavelengths $\lambda = 2\pi/k = 2$–4 cm satisfying the deep-water approximation $\tanh(kh) \simeq 1$. In the first experiment, we interfered $N = 3$ plane water waves with equal amplitudes and frequency $\omega/2\pi \simeq 6.8$ Hz (wavelength $\lambda \simeq 4$ cm, taking into account the surface-tension correction), but different directions $\mathbf{k}_i = \overline{\mathbf{x}}\cos\varphi_i + \overline{\mathbf{y}}\sin\varphi_i$, $\varphi_i = 2\pi(i-1)/N$, $i = 1, \ldots, N$, and phases $\phi_i = \varphi_i$ (Fig. 2a and Methods). The phases ϕ_i are inessential for the three-wave interference but make a difference in similar set-ups with $N > 3$ waves. We measured the water-surface elevation $\mathcal{Z}(x, y, t)$ using fast chequerboard demodulation (FCD)[42] (Methods).

Figure 2a shows the measured three-wave interference field $\mathcal{Z}(x, y, t = 0)$ inside the hexagonal cavity (see Supplementary Video 1 for its temporal evolution). The corresponding complex field $Z(x,y)$ was then obtained using the Hilbert transform (Fig. 2b). Notably, this field exhibits a hexagonal lattice of phase singularities (wave vortices)[1–6,38] with alternating topological charges $\ell = \pm 1$. These are points where the wave amplitude vanishes, $|Z| = 0$, whereas the phase $\mathrm{Arg}(Z)$ increases by $2\pi\ell$ when encircling the point in the anticlockwise direction in the (x,y) plane. Such wave vortices are the simplest topological entities in a scalar structured wave field. These purely classical objects somewhat resemble vortices in quantum fluids, for which the quantized circulation is associated with the phase increment of the wavefunction.

Our further consideration requires the full-vector wave field $\mathcal{R}(x, y, t)$. Although making direct measurements is challenging, the horizontal in-plane components can be reconstructed from the measured vertical component $\mathcal{Z}$ using the gravity-wave equations: $(X, Y) = k^{-1}\nabla_2 Z$, where $\nabla_2 = (\partial_x, \partial_y)$ is the in-plane gradient. This method is like reconstructing the three-dimensional surface-plasmon–polariton field from gradients of the measured vertical electric-field component[12,13,15] or acoustic three-dimensional velocity field from gradients of the measured scalar pressure field[11,41].

Figure 2c shows the colour- and brightness-coded distribution of the instantaneous three-dimensional displacement field $\mathcal{R}(x, y, t = 0)$ reconstructed from the three-wave interference measurements. Notably, it exhibits a hexagonal lattice of skyrmions: areas where the directions of unit vectors $\bar{\mathcal{R}}$ can be mapped onto the unit sphere, with opposite directions, $\bar{\mathcal{R}} = \overline{\mathbf{z}}$ in the centre and $\bar{\mathcal{R}} = -\overline{\mathbf{z}}$ in the vertexes. The topological number of this mapping (not related to the topological vortex number ℓ) is $Q = \frac{1}{4\pi}\iint \bar{\mathcal{R}} \cdot (\partial_x \bar{\mathcal{R}} \times \partial_y \bar{\mathcal{R}})\, \mathrm{d}x\, \mathrm{d}y = 1$ at $t = 0$, and its sign flips after a half-period of wave oscillations. Akin to vortices, skyrmions are topologically stable structures; however, unlike point-like phase singularities in a scalar field, skyrmions are continuously distributed vector-field textures. In our experiment, the hexagonal skyrmion boundary was noticeably perturbed (we determined it to be a local minimum curve for $\overline{\mathcal{Z}}(x, y, 0)$), but the calculated topological number $Q \simeq 1$ with an accuracy of 10^{-2}. Thus, we generated water-wave skyrmions, which resemble the recently observed optical[12,14,16,19] and acoustic[11,17,18] skyrmions, typically using $N = 6$ interfering waves.

Next, we analysed the local elliptical polarizations (trajectories) traced by the experimentally retrieved displacement field $\mathcal{R}(x, y, t)$ and the corresponding spin density $\mathbf{S}(x,y)$. The distribution of the normalized spin vectors $\bar{\mathbf{S}}(x, y)$ is shown in Fig. 2d. For an ideal three-wave interference pattern, they form a lattice with triangular meron (half-skyrmion) cells[15,19,38]. Each triangular cell is centred around the phase singularity of $Z(x,y)$, where the spin is directed vertically, $\bar{\mathbf{S}} = \ell\overline{\mathbf{z}}$, whereas the boundaries correspond to $S_z = 0$. Such merons are mapped onto the upper or lower hemisphere of spin directions with

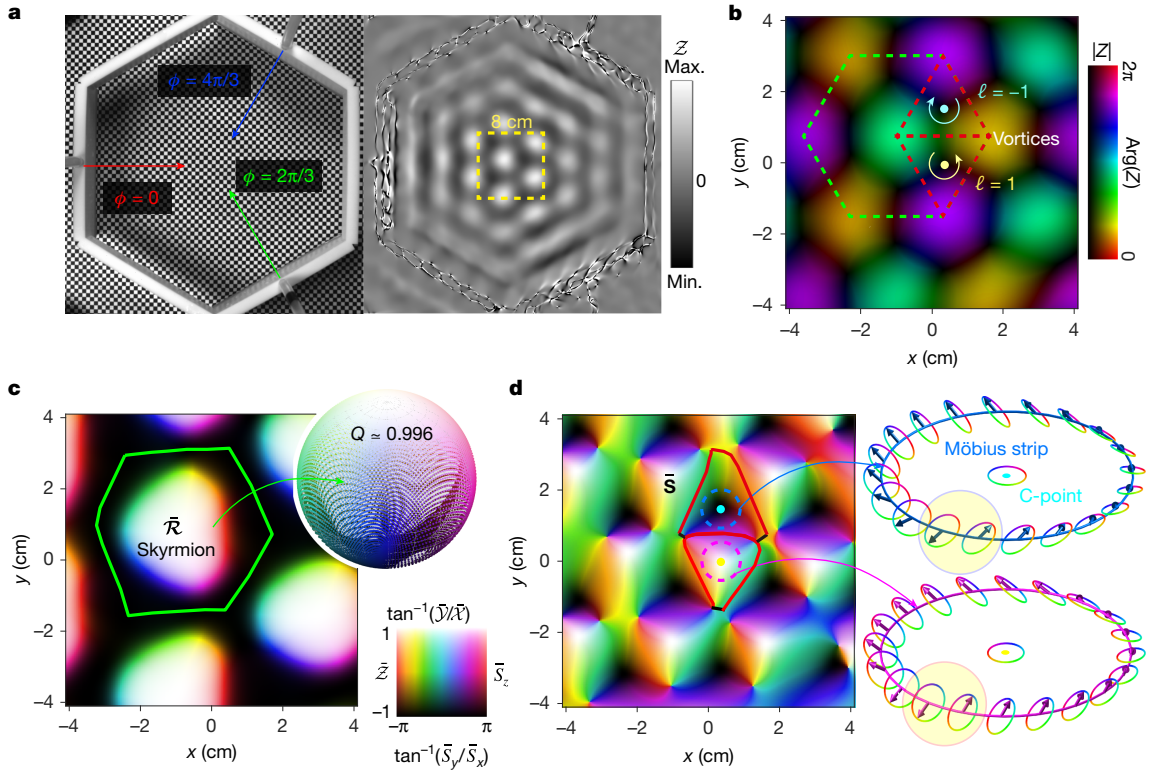

Fig. 2 | Topological structures in the interference patterns of three water waves. a, Experimental set-up for generating three plane waves with the same amplitude and frequency but different azimuthal angles of propagation $\varphi = (0, 2\pi/3, 4\pi/3)$ and the corresponding phases delays $\phi = \varphi$. The measured vertical displacement field $\mathcal{Z}(x, y, t = 0)$ is shown on the right. **b**, Distributions of the amplitude (brightness) and phase (colour) of the corresponding complex field $Z(x,y)$ in the rectangular area indicated by the yellow square in **a**. Examples of phase singularities (wave vortices) with topological charges $\ell = \pm 1$ are shown by dots and circular arrows indicating the $2\pi\ell$ phase increments around these. **c**, Distribution of the reconstructed three-dimensional displacement field $\mathcal{R}(x, y, t = 0)$ (encoded by the brightness and colours) exhibits skyrmions. The field directions in the near-hexagonal cell are mapped onto the unit sphere with the topological number $Q = 1$. The measured skyrmion boundary is noticeably perturbed compared to the ideal hexagon shown in **b**, but the topological charge Q calculated from the discrete experimental data is very close to the theoretical integer value. **d**, Corresponding distribution of the spin density $\mathbf{S}(x,y)$ exhibits a lattice of near-triangular 'failed' merons (half-skyrmions). The meron boundaries determined by $S_z(x, y) = 0$ (red curves) are not closed, unlike the ideal triangles in **b**. Nonetheless, these quasi-merons contain stable topological structures in the distributions of elliptical polarizations (trajectories) traced by the displacement field $\mathcal{R}(x, y, t)$. These are C-points of purely circular polarizations surrounded by polarization Möbius strips. The orientations of the major semiaxes of the polarization ellipses (blue and magenta vectors) flip (highlighted in yellow) as they continuously encircle the C-point. Max., maximum; min., minimum.

the corresponding topological numbers $Q_S = \ell/2$ (Methods). However, these spin merons are not topologically stable, because the vertexes of the triangles correspond to higher-order singular points with $\mathbf{S} = 0$. In a real perturbed system, such as our experiment, these singular points split, the perturbed $S_z = 0$ lines do not form closed boundaries and the spin merons fail (Fig. 2d and Methods).

Nonetheless, elliptical polarizations $\mathcal{R}(x, y, t)$ exhibit another kind of topologically stable structures. Namely, centres of the broken spin-meron triangles contain polarization singularities: C-points with purely circular polarization[3,7,10]. Orientations of the major semiaxes of three-dimensional polarization ellipses around C-points form polarization Möbius strips. The semiaxis direction flips when continuously encircling the polarization singularity[8,10]. These topological structures have previously been observed in optical[9] and acoustic[11] fields and were recently predicted[37] for water waves. Figure 2d shows the polarization Möbius strips around two C-points (approximately corresponding to phase singularities of $Z(x,y)$) retrieved from our experimental measurements of the three-wave interference field.

Note that earlier works[28,34,35] described a square lattice of alternating first-order water-wave vortices in the interference patterns of two orthogonal π/2-phase-shifted standing waves, which is equivalent to $N = 4$ waves with $\phi_i = \varphi_i$. However, such a configuration produces neither displacement skyrmions nor polarization Möbius strips (Methods).

Bessel vortices with different topological charges

In the second experiment, we generated water-wave vortices with different topological charges. We interfered $N = 24$ water waves with the same amplitudes, frequency $\omega/2\pi \simeq 9$ Hz (wavelength $\lambda \simeq 2.7$ cm), circularly distributed directions $\varphi_i = 2\pi(i-1)/N$, $i = 1, \ldots, N$, and phases $\phi_i = \ell\varphi_i$ corresponding to the topological charge $\ell \in \mathbb{Z}$ (Fig. 3 and Methods). In the $N \gg 1$ limit, this interference produces circularly symmetric Bessel-type water-wave vortices[38,43,44], like electromagnetic surface plasmon–polariton vortices[45,46].

We measured the vertical displacement field $\mathcal{Z}(x, y, t)$ with FCD. Figure 3a shows the measured field for $\ell = 2$ at $t = 0$. The corresponding complex fields $Z(x,y)$ for $\ell = 0, 1, 2, 8$ are shown in Fig. 3b,c (see also Supplementary Videos 2–5 for the temporal evolution of $\mathcal{Z}(x, y, t)$). These fields correspond to the Bessel-type vortices $Z \propto J_\ell(kr)\exp(\mathrm{i}\ell\varphi)$ (J_ℓ is the Bessel function) with $2\pi\ell$ phase increment around the centre[38,43]. (Notably, the three-dimensional displacement field $\mathcal{R}(x, y, t = 0)$ of the $\ell = 0$ non-vortex mode forms a skyrmion in the centre; Methods). For $\ell \neq 0$, these are quasi-standing waves that do not propagate in the radial direction but do propagate in the azimuthal direction. The wave amplitude is maximum near the first Bessel-maximum ring of radius $r_{max} \simeq \sqrt{\ell}\lambda/2$. Thus, we demonstrated the controllable generation of higher-order water-wave vortices.

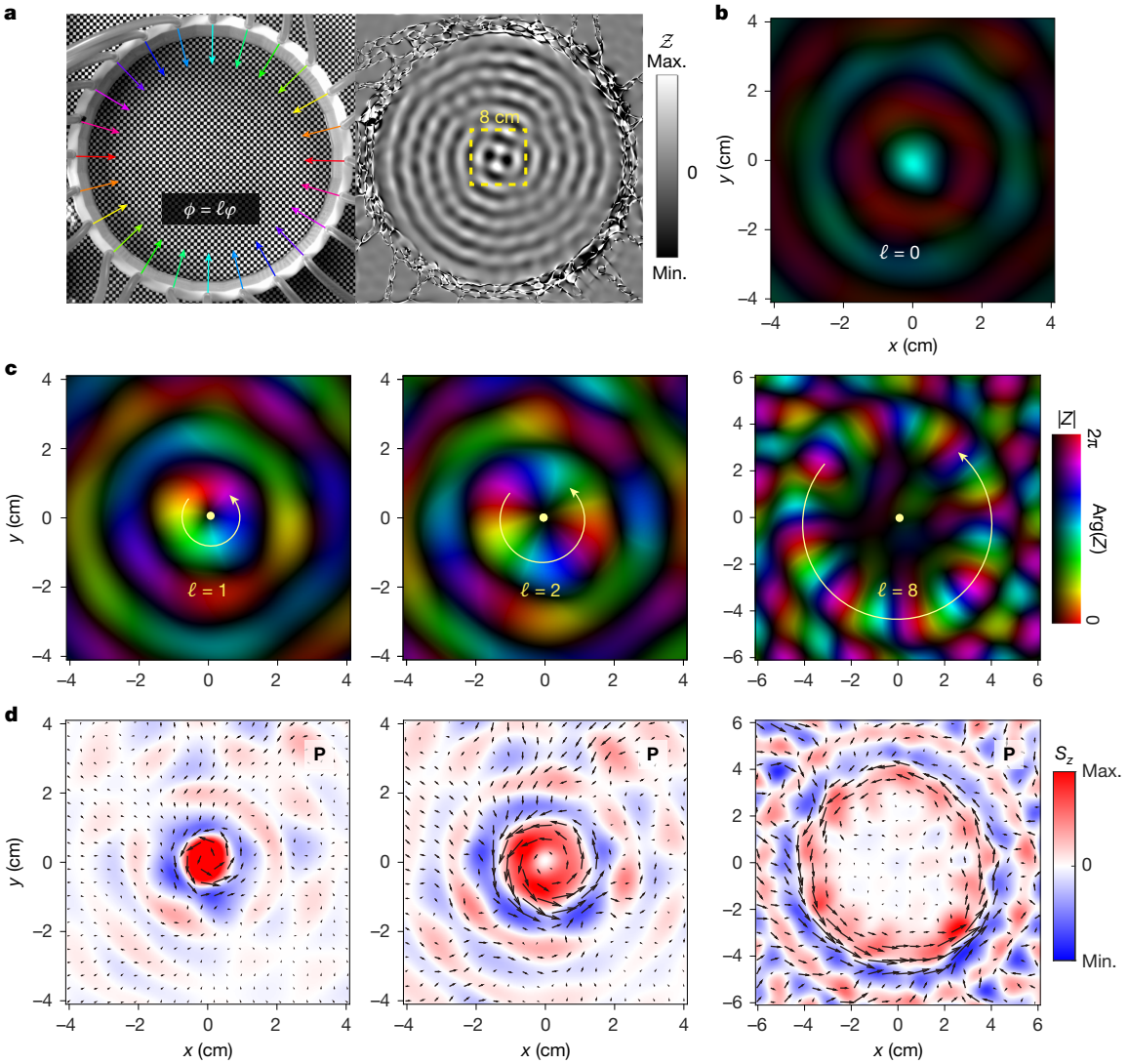

Fig. 3 | Generating Bessel-type water-wave vortices with different topological charges. a, Experimental set-up with $N = 24$ sources uniformly distributed around a circle with azimuthal phase difference $\phi = \ell\varphi$ corresponding to the integer topological charge ℓ (here $\ell = 2$ is shown). The measured vertical displacement field $\mathcal{Z}(x, y, t = 0)$ is shown on the right. **b**,**c**, Distributions of the amplitude (brightness) and phase (colour) of the reconstructed complex field $Z(x,y)$ for $\ell = 0$ (**b**) and $\ell = 1, 2, 8$ (**c**). **d**, Distributions of the time-averaged vertical spin density $S_z(x, y)$ (colour density plots) and in-plane wave momentum density $\mathbf{P}(x,y)$ (black vectors) for the Bessel vortices shown in **c**.

Such wave vortices have notable dynamical properties carrying both spin and OAM, so that the z component of the total angular momentum (spin plus orbital) is quantized according to the topological number ℓ (ref. 38). To quantify these angular-momentum properties, we reconstructed the complex three-dimensional displacement field $\mathbf{R}(x,y)$, as in the three-wave experiment. Then we calculated the corresponding spin density $\mathbf{S}(x,y)$ and the canonical wave momentum density $\mathbf{P}(x, y) = (\rho\omega/2)\mathrm{Im}[\mathbf{R}^* \cdot (\nabla_2)\mathbf{R}]$. This momentum density is directly related by the velocity $\mathbf{U}_S$ of the Stokes drift of water-surface particles, $\mathbf{P} = \rho\mathbf{U}_S$, which appears as a time-averaged nonlinear (quadratic) correction to their linear oscillatory motion[28,32,35,47,48]. The z component of the OAM density is described by the azimuthal component of the momentum density[38]: $L_z = (\mathbf{r} \times \mathbf{P})_z = rP_\varphi$.

Figure 3d displays the distributions of the vertical spin density S_z and the wave momentum density $\mathbf{P}$ calculated from the experimentally measured Bessel vortices with $\ell = 1, 2, 8$. One can see strong azimuthal momentum P_φ around the first Bessel-maximum ring, as well as rings of positive and negative spin S_z around it. (Similar momentum density distributions and the Stokes drift of fluid particles have been measured in acoustic Bessel beams[49]). Flipping the vortex sign $\mathrm{sgn}(\ell)$ results in the sign flipping for both the azimuthal momentum P_φ and spin S_z, which can be associated with spin–momentum locking in water waves. For the first-order vortices, $\ell = 1$, the spin density S_z reaches its maximum or minimum in the vortex centre $r = 0$, like the vertical-spin extrema near the first-order vortices and C-points in the three-wave interference (Fig. 2). In the next section we describe manifestations of these dynamical properties in the interactions between structured water waves and floating particles.

Trapping and manipulating floating particles

In these experiments, we used subwavelength, spherical, polyethylene particles with densities $\rho_p = 0.89$–0.96 g cm^{-3} and radii $a = 2.4, 3.1, 4.75$ and 6.35 mm, as well as a ping-pong ball with $a = 20$ mm, floating on the water surface. Such floating particles undergo fast oscillatory motion with the wave frequency ω, along with the slow time-averaged action of the wave field, which is quadratic in the field amplitude. This action is like the optical and acoustic radiation forces and torques underpinning optical and acoustic manipulation[22–25].

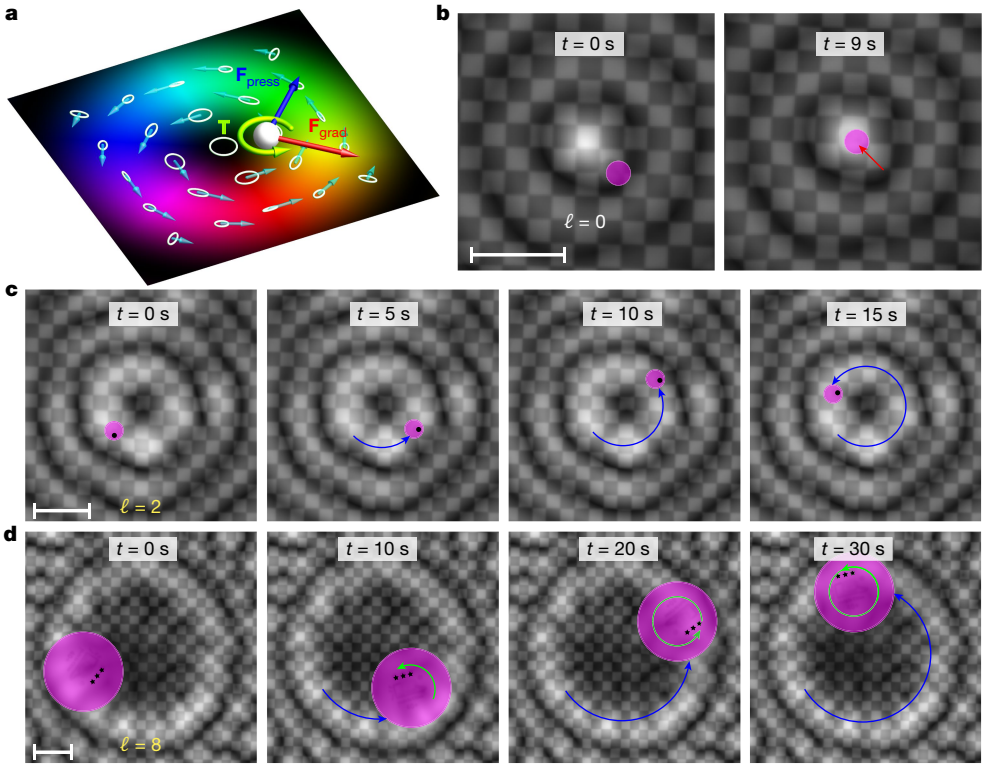

Fig. 4 | Dynamics of floating particles in the Bessel-vortex water waves. **a**, Schematic showing the radial gradient and azimuthal wave-pressure forces and the spin-induced torque, as described by equation (1). **b**, Trapping of the $a = 2.4$ mm particle in the central intensity maximum of the $\ell = 0$ mode provided by the radial gradient force. **c**, Radial trapping of the $a = 3.1$ mm particle in the first Bessel maximum of the $\ell = 2$ vortex, accompanied by its orbital motion due to the azimuthal wave-pressure force (compare with the wave-momentum distribution in Fig. 3d). **d**, Similar trapping and orbital motion of a ping-pong ball, $a = 20$ mm, in the $\ell = 8$ vortex. The ball also experiences spinning rotation (green arrows and the three-star markers) induced by the torque due to the spin density S_z and due to the radial gradient of the azimuthal wave-pressure force. In **b**–**d**, for better visibility, the actual video frames of floating particles with the chequerboard background are overlapped with the experimentally measured wave amplitude $|Z(x,y)|$ (greyscale), whereas the particle position and orientation are highlighted by the magenta and black markers. Scale bars, 2 cm.

Employing the analogy with optical and acoustic forces and torques[40,50,51], we introduced a toy model for the water-wave-induced force and torque on a floating particle. This model is based on the wave momentum density $\mathbf{P}$, spin density $\mathbf{S}$ and kinetic energy density (intensity) $W = \rho\omega^2|\mathbf{R}|^2/4$. Assuming the lowest-order dipole-like coupling between the water-wave field and the particle, which is quantified by the complex scalar polarizability α, the wave-induced force and torque on the particle can be written as (Methods):

$$\mathbf{F} = \mathrm{Re}(\alpha)\nabla_2 W + \omega\,\mathrm{Im}(\alpha)\mathbf{P} \equiv \mathbf{F}_{\mathrm{grad}} + \mathbf{F}_{\mathrm{press}},$$
$$T_{\mathrm{spin}} = \omega\,\mathrm{Im}(\alpha)S_z. \qquad (1)$$

Here we describe the action affecting the two-dimensional motion of the particle in the (x,y) plane: the horizontal in-plane force and the vertical z-directed torque. The first force term in equation (1) is the gradient force responsible for trapping particles in high-intensity (for $\mathrm{Re}(\alpha) > 0$) or low-intensity ($\mathrm{Re}(\alpha) < 0$) zones, whereas the second term is the wave-pressure force directed along the local wave momentum.

In optics and acoustics, in the small-particle limit $ka \ll 1$, the polarizability typically scales proportionally to the particle volume: $\alpha \propto a^3$, and the imaginary part $\mathrm{Im}(\alpha)$ characterizes the absorption of waves by a particle. Therefore, the wave-pressure force and spin-induced torque in equation (1) can be associated with the transfer of momentum and spin angular momentum from the wave to the particle[40,50,51].

Figure 4a schematically shows the action of the gradient force, the wave-pressure force and the spin-induced torque (equation (1)) on a particle in a water-wave vortex. The gradient and wave-pressure forces are directed radially and azimuthally, according to the intensity and phase gradients, whereas the torque is induced by the local elliptical polarizations (trajectories) of water-surface particles in the (x,y) plane.

Figure 4b–d (see also Supplementary Videos 6–9) displays the observed dynamics of floating particles of different sizes in the Bessel-vortex water waves with different topological charges ℓ (Fig. 3). First, a particle with $a = 2.4$ mm is attracted to the centre of the $\ell = 0$ Bessel wave and is trapped there (Fig. 4b and Supplementary Video 6). This is clear evidence of the radial gradient force corresponding to $\mathrm{Re}(\alpha) > 0$. (This is somewhat counterintuitive because in acoustics, $\mathrm{Re}(\alpha) < 0$ for $\rho_p < \rho$, where ρ_p is the particle density). Second, for the $\ell = 2$ vortex, a particle with $a = 3.1$ mm is trapped in the first Bessel-maximum ring, and we observe its orbital motion due to the azimuthal wave-pressure force (Fig. 4c and Supplementary Video 7). This is a direct mechanical manifestation of the OAM L_z carried by water-wave vortices and transferred to the particle. (The particle reaches a constant angular velocity when the azimuthal pressure force is balanced by the friction, which is proportional to the velocity). Third, we observed similar radial trapping and orbital motion for a ping-pong ball ($a = 20$ mm) in a water-wave vortex with $\ell = 8$ (Fig. 4d and Supplementary Video 9). Notably, the ping-pong ball also experiences a spinning rotation, which is caused by the water-wave-induced torque T with respect to the ball centre. The angular velocities of the spinning and orbital rotations are $\Omega_{\mathrm{spin}} \simeq 2\Omega_{\mathrm{orb}} \simeq \pi/10\,\mathrm{rad\,s^{-1}}$ (much less than ω). This torque can have two origins: (1) the spin-induced torque T_{spin} of equation (1) (note the positive spin density $S_z > 0$ at the inner part of the Bessel ring, where the ball is trapped; Fig. 3d) and (2) the 'gradient torque' T_{grad}, which originates from the radial gradient of the azimuthal wave-pressure force and strongly pushes the outer side of the ball.

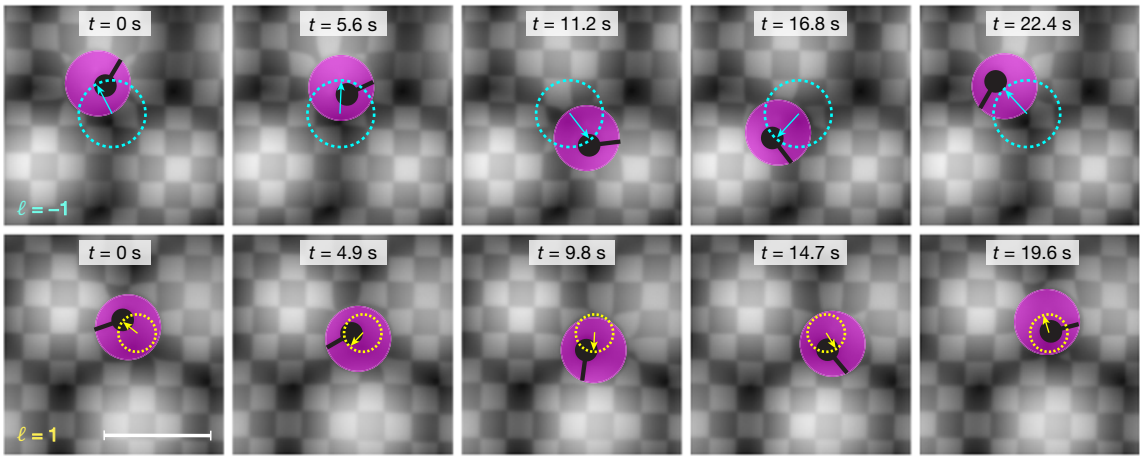

Fig. 5 | Dynamics of floating particles around the first-order vortices in the three-wave interference lattice. Particles of radius $a = 6.35$ mm are placed near the $\ell = \pm 1$ vortices shown in Fig. 2b,d. The particles are trapped within the triangular quasi-spin-meron zones and experience orbital and spinning rotations. These rotations are non-uniform because of the circularly asymmetric character of the vortices and are shown as the approximate circular trajectories of the particle centres (dashed circles). Black markers indicate the particle orientation.

Both of these torques act in the same direction and contribute to the spinning rotation (Methods).

The observed dynamics is entirely like that of the radial trapping and orbital and spinning motion of small particles in optical vortex fields[52,53]. The only difference is that, in optics, the spinning motion can be controlled by the global circular polarization of the wave, independently of the vortex charge ℓ, whereas in water waves, the signs of the orbital and spinning rotations are locked with each other. Note that the radial gradient force is not always sufficient for stable trapping: particles of certain sizes can escape the vortex ring when the centrifugal force prevails (Supplementary Video 8). This effect can be employed to measure the trapping force.

We finally show that such water-wave manipulations of floating particles are robust and do not require circularly symmetric Bessel vortices. We placed particles of radius $a = 6.35$ mm near the centres of the $\ell = \pm 1$ vortices in the three-wave interference lattice (Fig. 2). Figure 5 (see also Supplementary Videos 10 and 11) shows that the particles are trapped around such vortices within the quasi-spin-meron triangular zones. Furthermore, the particles undergo both orbital and spinning rotations with the directions controlled by $\mathrm{sgn}(\ell)$ and angular velocities $\Omega_{\mathrm{orb}} \simeq 2\Omega_{\mathrm{spin}} \simeq \pi/10$ rad s^{-1}. The spinning motion can be induced by the two kinds of torques mentioned above, particularly by the maximum/minimum spin density S_z in the centres (C points) of the quasi-spin-meron zones (Fig. 3d and Methods).

Conclusions

We have demonstrated the controllable generation of topological water-wave structures, including vortices with different topological charges, skyrmions and polarization Möbius strips. Our experiments evidence the robustness of these structures, in contrast, for example, to spin merons 'broken' in a perturbed three-wave interference pattern. Most importantly, we have revealed the notable dynamical properties of these structured water waves and demonstrated their capability to manipulate floating particles of different sizes, including stable trapping and orbital and spinning rotations.

Our results provide a new platform for wave-induced mechanics, which can extrapolate the well-developed optical and acoustic manipulations to fluid mechanics. In particular, capillary water waves can be employed for the microfluidic manipulation of biomedical objects, like the presently used acoustic waves[24,25,54]. Although optical manipulation uses wavelengths of the order of micrometres and acoustic manipulation the wavelength range from the tens of micrometres to millimetres, water waves can efficiently use the next range from millimetres to centimetres and even beyond to colossal ocean waves.

This work is only the first step in this direction. Further development may include a detailed consideration of the interaction between structured water waves and floating particles, the sorting of particles with different properties using water waves, the interplay between topology and nonlinearity inherent in water waves, a consideration of multi-frequency and spatio-temporal structured water waves and so forth.

Online content

Any methods, additional references, Nature Portfolio reporting summaries, source data, extended data, supplementary information, acknowledgements, peer review information; details of author contributions and competing interests; and statements of data and code availability are available at https://doi.org/10.1038/s41586-024-08384-y.

1. Nye, J. F. & Berry, M. V. Dislocations in wave trains. *Proc. R. Soc. Lond. A* **336**, 165–190 (1974).
2. Soskin, M. S. & Vasnetsov, M. V. Singular optics. *Prog. Opt.* **42**, 219–276 (2001).
3. Dennis, M. R., O'Holleran, K. & Padgett, M. J. Singular optics: optical vortices and polarization singularities. *Prog. Opt.* **53**, 293–363 (2009).
4. Shen, Y. et al. Optical vortices 30 years on: OAM manipulation from topological charge to multiple singularities. *Light Sci. Appl.* **8**, 90 (2019).
5. Guo, S., Ya, Z., Wu, P. & Wan, M. A review on acoustic vortices: generation, characterization, applications and perspectives. *J. Appl. Phys.* **132**, 210701 (2022).
6. Bliokh, K. Y. et al. Theory and applications of free-electron vortex states. *Phys. Rep.* **690**, 1–70 (2017).
7. Nye, J. F. & Hajnal, J. V. The wave structure of monochromatic electromagnetic radiation. *Proc. R. Soc. Lond. A* **409**, 21–36 (1987).
8. Freund, I. Optical Möbius strips in three-dimensional ellipse fields. I. Lines of circular polarization. *Opt. Commun.* **283**, 1–15 (2010).
9. Bauer, T. et al. Observation of optical polarization Möbius strips. *Science* **347**, 964–966 (2015).
10. Bliokh, K. Y., Alonso, M. A. & Dennis, M. R. Geometric phases in 2D and 3D polarized fields: geometrical, dynamical, and topological aspects. *Rep. Prog. Phys.* **82**, 122401 (2019).
11. Muelas-Hurtado, R. D. et al. Observation of polarization singularities and topological textures in sound waves. *Phys. Rev. Lett.* **129**, 204301 (2022).
12. Tsesses, S. et al. Optical skyrmion lattice in evanescent electromagnetic fields. *Science* **361**, 993–996 (2018).
13. Du, L., Yang, A., Zayats, A. V. & Yuan, X. Deep-subwavelength features of photonic skyrmions in a confined electromagnetic field with orbital angular momentum. *Nat. Phys.* **15**, 650–654 (2019).
14. Davis, T. J. et al. Ultrafast vector imaging of plasmonic skyrmion dynamics with deep subwavelength resolution. *Science* **368**, eaba6415 (2020).
15. Dai, Y. et al. Plasmonic topological quasiparticle on the nanometre and femtosecond scales. *Nature* **588**, 616–619 (2020).
16. Deng, Z.-L., Shi, T., Krasnok, A., Li, X. & Alù, A. Observation of localized magnetic plasmon skyrmions. *Nat. Commun.* **13**, 8 (2022).

17. Ge, H. et al. Observation of acoustic skyrmions. *Phys. Rev. Lett.* **127**, 144502 (2021).
18. Cao, L., Wan, S., Zeng, Y., Zhu, Y. & Assouar, B. Observation of phononic skyrmions based on hybrid spin of elastic waves. *Sci. Adv.* **9**, eadf3652 (2023).
19. Shen, Y. et al. Optical skyrmions and other topological quasiparticles of light. *Nat. Photon.* **18**, 15–25 (2024).
20. Allen, L., Barnett, S. M. & Padgett, M. J. (eds) *Optical Angular Momentum* (IoP Publishing, 2003).
21. Andrews, D. L. & Babiker, M. (eds) *The Angular Momentum of Light* (Cambridge Univ. Press, 2012).
22. Grier, D. G. A revolution in optical manipulation. *Nature* **424**, 810–816 (2003).
23. Gao, D. et al. Optical manipulation from the microscale to the nanoscale: fundamentals, advances and prospects. *Light Sci. Appl.* **6**, e17039 (2017).
24. Ozcelik, A. et al. Acoustic tweezers for the life sciences. *Nat. Methods* **15**, 1021–1028 (2018).
25. Dholakia, K., Drinkwater, B. W. & Ritsch-Marte, M. Comparing acoustic and optical forces for biomedical research. *Nat. Rev. Phys.* **2**, 480–491 (2020).
26. Rozenman, G. G., Fu, S., Arie, A. & Shemer, L. Quantum mechanical and optical analogies in surface gravity water waves. *Fluids* **4**, 96 (2019).
27. Han, L., Chen, S. & Chen, H. Water wave polaritons. *Phys. Rev. Lett.* **128**, 204501 (2022).
28. Bliokh, K. Y., Punzmann, H., Xia, H., Nori, F. & Shats, M. Field theory spin and momentum in water waves. *Sci. Adv.* **8**, eabm1295 (2022).
29. Zhu, S. et al. Controlling water waves with artificial structures. *Nat. Rev. Phys.* **6**, 231–245 (2024).
30. Rubinsztein-Dunlop, H. et al. Roadmap on structured light. *J. Opt.* **19**, 013001 (2016).
31. Bliokh, K. Y. et al. Roadmap on structured waves. *J. Opt.* **25**, 103001 (2023).
32. Falkovich, G. *Fluid Mechanics* 2nd edn (Cambridge Univ. Press, 2018).
33. Bacot, V., Labousse, M., Eddi, A., Fink, M. & Fort, E. Time reversal and holography with spacetime transformations. *Nat. Phys.* **12**, 972–977 (2016).
34. Filatov, S. V. et al. Nonlinear generation of vorticity by surface waves. *Phys. Rev. Lett.* **116**, 054501 (2016).
35. Francois, N., Xia, H., Punzmann, H., Fontana, P. W. & Shats, M. Wave-based liquid-interface metamaterials. *Nat. Commun.* **8**, 14325 (2017).
36. Che, Z. et al. Generation of spatiotemporal vortex pulses by resonant diffractive grating. *Phys. Rev. Lett.* **132**, 044001 (2024).
37. Bliokh, K. Y. et al. Polarization singularities and Möbius strips in sound and water-surface waves. *Phys. Fluids* **33**, 077122 (2021).
38. Smirnova, D. A., Nori, F. & Bliokh, K. Y. Water-wave vortices and skyrmions. *Phys. Rev. Lett.* **132**, 054003 (2024).
39. Jones, W. L. Asymmetric wave-stress tensors and wave spin. *J. Fluid Mech.* **58**, 737–747 (1973).
40. Bliokh, K. Y. & Nori, F. Transverse and longitudinal angular momenta of light. *Phys. Rep.* **592**, 1–38 (2015).
41. Shi, C. et al. Observation of acoustic spin. *Natl Sci. Rev.* **6**, 707–712 (2019).
42. Wildeman, S. Real-time quantitative schlieren imaging by fast Fourier demodulation of a checkered backdrop. *Exp. Fluids* **59**, 97 (2018).
43. Ceperley, P. H. Rotating waves. *Am. J. Phys.* **60**, 938–942 (2010).
44. Wang, H., Szekerczes, K. & Afanasev, A. Electromagnetic vortex topologies from sparse circular phased arrays. *J. Phys. Commun.* **6**, 025005 (2022).
45. Ohno, T. & Miyanishi, S. Study of surface plasmon chirality induced by Archimedes' spiral grooves. *Opt. Express* **14**, 6285–6290 (2006).
46. Kim, H. et al. Synthesis and dynamic switching of surface plasmon vortices with plasmonic vortex lens. *Nano Lett.* **10**, 529–536 (2010).
47. van den Bremer, T. S. & Breivik, Ø. Stokes drift. *Philos. Trans. R. Soc. A* **376**, 20170104 (2017).
48. Abella, A. P. & Soriano, M. N. Measurement of Eulerian vorticity beneath rotating surface waves. *Phys. Scr.* **95**, 085007 (2020).
49. Hong, Z., Zhang, J. & Drinkwater, B. W. Observation of orbital angular momentum transfer from Bessel-shaped acoustic vortices to diphasic liquid-microparticle mixtures. *Phys. Rev. Lett.* **114**, 214301 (2015).
50. Bliokh, K. Y., Bekshaev, A. Y. & Nori, F. Extraordinary momentum and spin in evanescent waves. *Nat. Commun.* **5**, 3300 (2014).
51. Toftul, I. D., Bliokh, K. Y., Petrov, M. I. & Nori, F. Acoustic radiation force and torque on small particles as measures of the canonical momentum and spin densities. *Phys. Rev. Lett.* **123**, 183901 (2019).
52. O'Neil, A. T., MacVicar, I., Allen, L. & Padgett, M. J. Intrinsic and extrinsic nature of the orbital angular momentum of a light beam. *Phys. Rev. Lett.* **88**, 053601 (2002).
53. Garcés-Chávez, V. et al. Observation of the transfer of the local angular momentum density of a multiringed light beam to an optically trapped particle. *Phys. Rev. Lett.* **91**, 093602 (2003).
54. Ding, X. et al. Surface acoustic wave microfluidics. *Lab Chip* **13**, 3626–3649 (2013).

Methods

Experimental set-up and FCD

In the three-wave interference experiment, we used the set-up shown in Fig. 2a. The interference field was produced within a three-dimensional-printed hexagonal structure with 16-cm-wide sides, where three sides (1, 3 and 5) acted as independent plane-wave sources, whereas the opposite sides (2, 4 and 6) were open boundaries (raised above the water surface). The whole structure was surrounded by sponge absorbers to prevent wave reflections. The source sides were connected with tubing to speakers controlled by a multichannel sound card (Quantum 4848, Presonus), which was externally interfaced with a computer. We used a sinusoidal signal with a frequency of $\omega/2\pi \simeq 6.8$ Hz corresponding to the gravity wavelength $\lambda \simeq 4$ cm. In the dispersion relation, we had to take into account the surface-tension correction, $\omega^2 = gk + (\sigma/\rho)k^3$, where σ is the surface-tension coefficient[32].

In the Bessel-vortex experiment, we used a three-dimensional-printed 24-gon structure, which approximated a circle of radius 18 cm (Fig. 3a). The 24 sides were connected by tubing to speakers controlled by a multichannel sound card, which provided coherent sources with computer-controlled amplitudes and phases. We used a sinusoidal signal with a frequency of $\omega/2\pi \simeq 9$ Hz corresponding to the wavelength $\lambda \simeq 2.7$ cm. As the wave amplitude decayed considerably over the diameter of the structure, we neglected reflections from opposite sides and the resonant condition for the wave double-passing the cavity.

In both of the above set-ups, we measured the water-surface elevation (vertical displacement) field $\mathcal{Z}(x, y, t)$ using FCD[42]. Namely, a chequerboard pattern (with black and white 0.5 × 0.5-cm^2 squares) was placed at the bottom of the transparent wave tank. A high-resolution video camera (Andor Zyla 5.5, 2,160 × 2,560 pixels, 100 fps), paired with a Canon 24–70 mm F2.8 L lens, was placed about 1.2 m above the wave tank to record the distortions to the chequerboard pattern caused by the wave. Compared to the undistorted reference pattern, a demodulation algorithm allowed us to recover the water-surface profile $\mathcal{Z}(x, y, t)$. Extended Data Fig. 1 shows examples of the field $\mathcal{Z}(x, y, t)$ reconstructed with FCD.

Topologically unstable spin merons in three-wave interference

An ideal interference pattern of three water waves with equal amplitudes and frequencies, propagating at angles $\varphi_i = 2\pi(i-1)/N, i = 1, 2, 3$, exhibits a triangular lattice of alternating merons in the spin density distribution $\mathbf{S}(x,y)$ (ref. 38). These are zones where the spin directions $\overline{\mathbf{S}}$ cover the upper or lower hemispheres with the corresponding half-integer topological numbers $Q_S = \frac{1}{4\pi}\iint \overline{\mathbf{S}} \cdot (\partial_x \overline{\mathbf{S}} \times \partial_y \overline{\mathbf{S}})\, dx\, dy = \pm 1/2$. These meron zones are separated by boundaries with $S_z = 0$ (Extended Data Fig. 2a).

However, this spin-meron lattice is topologically unstable because the vertexes of the triangles are degenerate points, where all the spin components vanish: $\mathbf{S} = 0$. Any generic, small perturbation splits these degenerate points into lower-order degeneracies. As a result, the boundaries $S_z = 0$ do not form closed meron zones. This is exactly what we observed in our experiment (Fig. 2d and Extended Data Fig. 2b). When we closed a near-triangular, non-closed contour $S_z = 0$ with missing fragments of the boundary, the spins inside these quasi-meron zones were mostly mapped onto the upper or lower hemispheres, but the corresponding topological numbers Q_S were not half-integer, as shown in Extended Data Fig. 2b.

By contrast, skyrmions formed by the three-dimensional displacement field $\mathcal{R}(x, y, t)$ are topologically stable. Their hexagonal boundaries can be deformed by a small perturbation of the field but remain closed with an integer topological charge Q (Fig. 2c).

Comparison with four-wave interference

In earlier works[28,34,35], the researchers generated a square lattice of alternating first-order water-wave vortices in the interference patterns of two orthogonal π/2-phase-shifted standing waves, which is equivalent to $N = 4$ plane waves with $\phi_i = \varphi_i$. We also generated such interference using a three-dimensional-printed square structure and frequency $\omega/2\pi \simeq 6.8$ Hz (wavelength $\lambda \simeq 4$ cm). Akin to the three-wave interference experiments, we used FCD to measure the vertical displacement field $\mathcal{Z}(x, y, t)$ and reconstruct the horizontal displacement-field components. Extended Data Fig. 3 shows that such four-wave interference exhibits the first-order vortices (phase singularities) in the complex field $Z(x,y)$ but contains neither skyrmions in the three-dimensional displacement field $\mathcal{R}(x, y, t)$ nor polarization Möbius strips around the centres of quasi-merons of the spin density $\mathbf{S}(x,y)$.

Skyrmion in the $\ell = 0$ Bessel mode

Figure 3 shows the distributions of the normalized instantaneous displacement vectors $\tilde{\mathcal{R}}(x, y, t = 0)$, as in Fig. 2c but for the generated Bessel modes. Notably, the non-vortex mode with $\ell = 0$ exhibits a skyrmion with $Q = 1$ in its centre (Extended Data Fig. 4a), whereas the vortex modes with $\ell \neq 0$ do not contain $\tilde{\mathcal{R}}$ skyrmions (Extended Data Fig. 4b).

Examples of unstable trapping of floating particles

In some cases, the trapping of floating particles in the high-intensity field zones can be unstable. Extended Data Fig. 5 and Supplementary Video 8 show the evolution of a particle with radius $a = 4.75$ mm in a Bessel-vortex water wave with $\ell = 2$. After being trapped and undergoing orbital rotation in the first Bessel-maximum ring for some time, the particle escapes the trap. This occurs when the radial centrifugal force $F_c = m\Omega_{orb}^2 r$ (m is the particle mass) is larger than the trapping gradient force F_{grad}.

In addition, Supplementary Video 10 shows that a particle with radius $a = 6.35$ mm trapped near the $\ell = -1$ vortex in the three-wave interference field also escapes the trap after some time. This does not happen for a similar particle near the $\ell = 1$ vortex (Supplementary Video 11). This can be caused by different initial conditions, which result in different velocities and orbits of particles in two similar traps (Fig. 5).

Water-wave-induced forces and torques on floating particles

Here we introduce a theoretical model based on the analogy between the main dynamical properties of monochromatic (single-frequency) optical, acoustic and water-wave fields[28,55]. These fields all have similar forms for the local energy, canonical momentum and spin density. Moreover, the main forces and torques on small isotropic particles have similar forms in optics and acoustics[51]. Therefore, it is natural to expect that there will be similar forces and torques for small floating particles interacting with a single-frequency water-wave field.

This approach is based on the minimum coupling between the lowest-order multipole moments induced at the particle by the incident wave field. In acoustics, these are the monopole and dipole moments associated, respectively, with uniform compression or expansion and with a linear displacement of the particle. These monopole and dipole moments naturally interact with the scalar-pressure and vector-velocity (or displacement) acoustic fields. For water waves, assuming an incompressible fluid and particle, it seems that only the dipole moment coupled to the vector displacement field should be relevant. However, in contrast to the bulk acoustic waves, surface water waves are highly anisotropic, so that their vertical (z) and horizontal (x,y) properties can differ dramatically. In fact, the water-wave equations are like the two-dimensional acoustic equations if we treat the vertical displacement Z as a scalar field (analogous to the acoustic pressure) and the horizontal displacement $\mathbf{R}_2 = (X, Y)$ as a two-dimensional vector field (analogous to the acoustic velocity)[28,56]. Moreover, note that vertical oscillations of a floating particle generate a monopole-like circularly symmetric water-wave field, whereas horizontal oscillations of the particle produce a dipole-like water-wave field propagating in the direction of oscillations but not in the orthogonal directions (Extended Data Fig. 6).

Thus, it is natural to characterize a floating particle by the monopole and dipole moments induced by the vertical and horizontal displacement wave fields:

$$M = \alpha_M Z, \quad \mathbf{D_2} = \alpha_D \mathbf{R_2}. \tag{2}$$

Here α_M and α_D are the complex monopole and dipole polarizabilities of the particle. To find these parameters, one has to solve an exact water-wave scattering problem, like the Mie problem in optics[57] and acoustics[58]. This is beyond the scope of this work, and we will use the polarizabilities as unknown proportionality parameters with dimensions of volume.

Assuming the minimal-coupling energy of the wave–particle interaction in the form

$$W_{\text{int}} = -\frac{\rho\omega^2}{2}\text{Re}(M^* Z + \mathbf{D_2^*}\cdot\mathbf{R_2}), \tag{3}$$

we obtain the wave-induced force on the particle[50,51,59]:

$$\mathbf{F} = \text{Re}(\alpha_M)\boldsymbol{\nabla}_2 W^{(z)} + \text{Re}(\alpha_D)\boldsymbol{\nabla}_2 W^{(x,y)} + \omega\text{Im}(\alpha_M)\mathbf{P}^{(z)} + \omega\text{Im}(\alpha_D)\mathbf{P}^{(x,y)}. \tag{4}$$

Here we introduced the parts of the kinetic energy density and of the wave momentum density related to the vertical and horizontal displacement fields: $W^{(z)} = (\rho\omega^2/4)|Z|^2$, $W^{(x,y)} = (\rho\omega^2/4)|\mathbf{R_2}|^2$, $\mathbf{P}^{(z)} = (\rho\omega/2)\text{Im}[Z^*\boldsymbol{\nabla}_2 Z]$ and $\mathbf{P}^{(x,y)} = (\rho\omega/2)\text{Im}[\mathbf{R_2^*}\cdot(\boldsymbol{\nabla}_2)\mathbf{R_2}]$. In this work, we need only the simplest toy model that can explain the main features of the particle behaviour in structured water-wave fields. Therefore, we set $\alpha_M = \alpha_D \equiv \alpha$, and in this case, equation (4) is reduced to the force in equation (1). It perfectly explains the particle dynamics observed in our experiments.

In turn, the vertical torque on a small particle involves only the dipole moment and can be derived as

$$T_{\text{spin}} = -\frac{\rho\omega^2}{2}\text{Re}(\mathbf{D_2^*}\times\mathbf{R_2}). \tag{5}$$

For $\alpha_D = \alpha$, this yields the second equation in equation (1).

This model assumes small subwavelength particles with $ka \ll 1$ and point-like induced monopoles and dipoles. For larger, finite-sized particles, another type of torque can appear because of the difference in the local wave-induced forces on opposite sides of the particle (see the next section).

Estimating torque, spin and orbital rotations of particles in experiments

We first consider rotations of a ping-pong ball in the Bessel-vortex field with $\ell = 8$ (Fig. 4d and Supplementary Video 9). This ball has diameter $2a = 4$ cm. The intensity-maximum ring containing most of the azimuthal momentum of the vortex has radius $r_{\max} \simeq 4$ cm and thickness $\Delta r_{\max} \simeq 2$ cm. The ball is trapped such that it occupies the radial range $r \in (1, 5)$ cm. Therefore, the wave-pressure force acts mostly on its outer part, whereas the inner part is in the low-intensity and low-momentum zone. This produces a torque with respect to the centre of the ball, which is caused by the radial gradient of the azimuthal wave-pressure force and can be estimated as $T_{\text{grad}} \sim F_{\text{press}} a = \omega\text{Im}(\alpha)P_\varphi a$.

The centre of the ping-pong ball is trapped around the maximum of the spin density S_z (around $r \simeq 3$ cm) (Fig. 3d). This can cause the spin-induced torque of equation (1): $T_{\text{spin}} = \omega\text{Im}(\alpha)S_z$. To compare T_{spin} and T_{grad}, note that the spin density is proportional to the wave intensity, and the azimuthal momentum density is proportional to the intensity multiplied by the phase gradient ℓ/r. Therefore, the ratio of the gradient and spin-induced torques can be estimated as

$$T_{\text{grad}}/T_{\text{spin}} \sim |\ell|a/r. \tag{6}$$

For small particles with $a \ll r$, the gradient torque is negligible. However, in the case under consideration, with $a \sim r$ and $\ell = 8$, the gradient torque dominates, so that the observed spinning of the ping-pong ball is apparently caused by this effect.

Let us now compare the spinning rotation due to the gradient torque with the orbital rotation caused by the azimuthal wave-pressure force. One can consider this orbital rotation in terms of the torque produced by the azimuthal wave-pressure force with respect to the vortex centre: $T_{\text{orb}} \simeq F_{\text{press}} r$, where r is the radius of the orbital trajectory of the ball. It is larger than the gradient torque T_{grad} because $r > a$. However, to compare the angular velocities of the spinning and orbital rotations, note that the moment of inertia of a particle with respect to its centre is $I_0 \sim ma^2$, whereas the moment of inertia with respect to the vortex centre is $I_1 \sim mr^2$. Therefore, comparing the angular accelerations, $\tau = T/I$, produced by the gradient and orbital torques, we obtain:

$$\tau_{\text{grad}}/\tau_{\text{orb}} \sim r/a. \tag{7}$$

This means that in terms of angular velocities, the spinning effect can prevail over the orbital rotation, exactly as we observe in Fig. 4d and Supplementary Video 9, with $\Omega_{\text{spin}} \simeq 2\Omega_{\text{orb}}$. Note that the ratio of these angular velocities can also be affected by the difference between the friction induced by the spinning and linear (orbital) motions of the particle, because the stationary velocities are determined by the balance between the wave-induced forces and torques and friction effects.

Finally, we consider the spin and orbital effects in the dynamics of particles with radius $a = 6.35$ mm in the $\ell = \pm 1$ vortices (Fig. 5 and Supplementary Videos 10 and 11). In this case, $a \sim r$ and $|\ell| = 1$, so that the gradient and spin-induced torques with respect to the particle centre are of the same order (equation (6)). Moreover, the particles are trapped within the triangular quasi-spin-meron zones with $S_z \propto \text{sgn}(\ell)$, including the spin density extrema in the centres, so the effect of the spin should be noticeable.

Let us estimate the effect of the spin-induced torque compared with the orbital motion induced by the azimuthal wave-pressure force. As these two effects are associated with the transfer of the spin and orbital angular momenta from the water-wave field to the particle, we estimate the spin and OAM in the wave-field zone occupied by the particle. Assuming for simplicity that the field has the Bessel-type form[38] with $\ell = 1$, we calculate the r-dependent spin and OAM densities:

$$\begin{aligned} S_z &\propto \frac{\rho\omega}{4}[J_0^2(kr) - J_2^2(kr)], \\ L_z &= rP_\varphi \propto \frac{\rho\omega}{2}[J_1^2(kr) + J_2^2(kr)]. \end{aligned} \tag{8}$$

where $J_n(kr)$ are the Bessel functions of the first kind. Calculating the ratio of the integral spin and OAM in the circular area with radius $2a$ (with the wavelength $\lambda = 2\pi/k = 40$ mm) around the vortex centre, we obtain:

$$\frac{\langle S_z\rangle}{\langle L_z\rangle} = \frac{\int_0^{2a} S_z(r)r\,\mathrm{d}r}{\int_0^{2a} L_z(r)r\,\mathrm{d}r} \simeq 0.55. \tag{9}$$

This ratio agrees with the observed ratio of the spinning and orbital angular velocities in this experiment: $\Omega_{\text{orb}} \simeq 2\Omega_{\text{spin}}$.

Thus, our simple theoretical model and estimates demonstrate very good agreement with the experimentally observed dynamics for a wide range of particles and field parameters. Therefore, we conclude that our approach captures the essential features of the interaction of structured water waves with floating particles.

Data availability

All data needed to evaluate the conclusions in the paper are present in the paper. Source data are provided with this paper.

55. Burns, L., Bliokh, K. Y., Nori, F. & Dressel, J. Acoustic versus electromagnetic field theory: scalar, vector, spinor representations and the emergence of acoustic spin. *New J. Phys.* **22**, 053050 (2020).
56. Meng, Y., Hao, Y., Guenneau, S., Wang, S. & Li, J. Willis coupling in water waves. *New J. Phys.* **23**, 073004 (2021).
57. Bohren, C. F. & Huffman, D. R. *Absorption and Scattering of Light by Small Particles* (Wiley, 1998).
58. Blackstock, D. T. *Fundamentals of Physical Acoustics* (Wiley, 2000).
59. Toftul, I. et al. Radiation forces and torques in optics and acoustics. Preprint at arxiv.org/abs/2410.23670 (2024).

Acknowledgements B.W., Z.C. and L.S. thank W. Liu for helpful discussions. This work was partially supported by the National Key Research and Development Program of China (Grant Nos. 2023YFA1406900 and 2022YFA1404800), the National Natural Science Foundation of China (Grant Nos. 12234007, 12321161645 and 12221004), a Major Program of the National Natural Science Foundation of China (Grant Nos. T2394480 and T2394481), the Science and Technology Commission of Shanghai Municipality (Grant Nos. 22142200400, 21DZ1101500, 2019SHZDZX01 and 23DZ2260100), the China Postdoctoral Science Foundation (Grant Nos. 2022M720810, 2022TQ0078, 2023M741024 and 2024T170218), a Nanyang Technological University Start-Up Grant, a Singapore Ministry of Education (MoE) AcRF Tier 1 grant (Grant No. RG157/23), a MoE AcRF Tier 1 Thematic grant (Grant No. RT11/23), the Imperial–Nanyang Technological University Collaboration Fund (Grant No. INCF-2024-007), Ikerbasque (Basque Foundation of Science), the Marie Skłodowska-Curie COFUND Programme of the European Commission (Project HORIZON-MSCA-2022-COFUND-101126600-SmartBRAIN3), the International Research Agendas Programme of the Foundation for Polish Science co-financed by the European Union under the European Regional Development Fund and the Teaming Horizon 2020 programme of the European Commission (ENSEMBLE3 Project No. MAB/2020/14), and the project of the Ministry of Science and Higher Education (Poland) 'Support for the activities of Centers of Excellence established in Poland under the Horizon 2020 programme' (Contract MEiN/2023/DIR/3797).

Author contributions Y.S., L.S., K.Y.B. and J.Z. conceived the basic idea behind the work and supervised its development. Z.C. and L.S. designed the experiments. Z.C. performed the experiments. B.W. and Z.C. analysed the experimental data. K.Y.B. prepared the first version of the manuscript with input from all authors. All authors took part in discussions, interpreting the results and revising the manuscript.

Competing interests The authors declare no competing interests.

Additional information

Supplementary information The online version contains supplementary material available at https://doi.org/10.1038/s41586-024-08384-y.

Correspondence and requests for materials should be addressed to Lei Shi, Yijie Shen, Konstantin Y. Bliokh or Jian Zi.

Peer review information *Nature* thanks Alexander Khanikaev, Sang Soon Oh and the other, anonymous, reviewer(s) for their contribution to the peer review of this work. Peer reviewer reports are available.

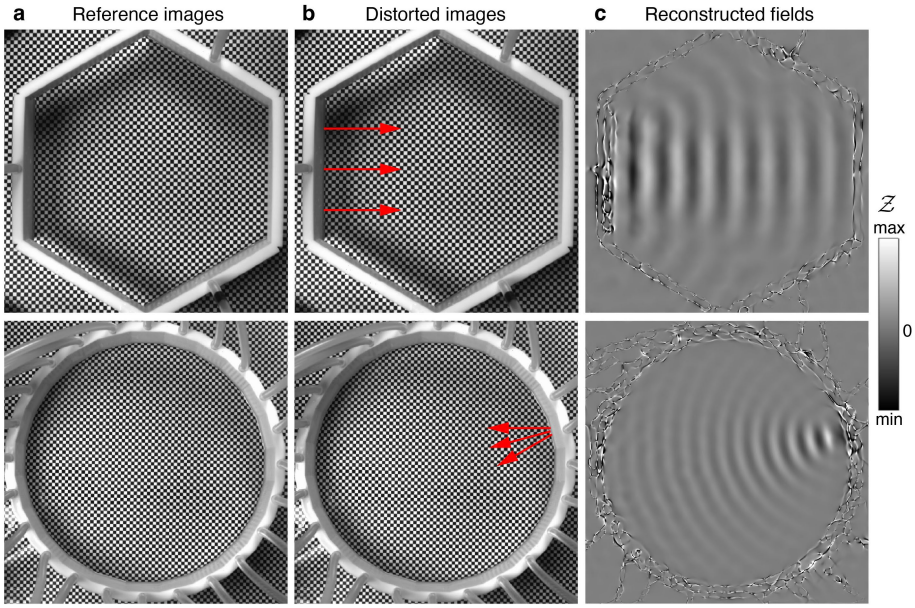

Extended Data Fig. 1 | Reconstruction of the vertical displacement field $\mathcal{Z}(x,y,t)$ via the FCD technique. Here we show a hexagonal structure for the three-wave interference, Fig. 2, where only one source side produces an x-propagating near-plane wave (upper row), and the 24-gonal structure for the Bessel-vortex generation, Fig. 3, where only one source generates a wave propagating towards the center of the structure (lower row). **a**, Reference images without waves. **b**, Distorted images in the presence of the wave at $t = 0$. **c**, Reconstructed field distributions $\mathcal{Z}(x, y, t = 0)$.

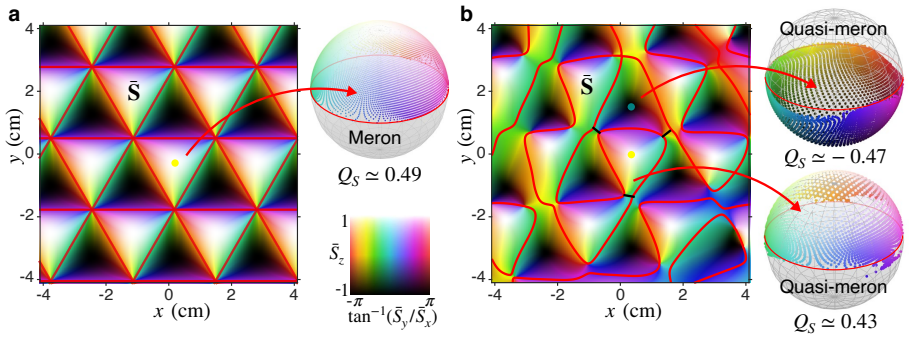

Extended Data Fig. 2 | Topologically unstable spin merons in three-wave interference. Shown are: distributions of the unit spin-density vectors $\bar{\mathbf{S}}(x, y)$, represented by brightness ($\bar{S}_z$) and color ($\tan^{-1}(\bar{S}_y/\bar{S}_x)$), the meron boundaries $S_z = 0$ (red curves), and mappings of the unit spin vectors in the merons onto the unit sphere, with the corresponding topological numbers Q_S. **a**, An ideal theoretically-predicted three-wave interference exhibiting a lattice of triangular alternating merons with $Q_S = \pm 1/2$. **b**, Perturbed three-wave interference field observed in our experiment (see Fig. 2). The curves $S_z = 0$ do not form closed meron areas. Closing the gaps with black lines and mapping the unit spin vectors onto the unit sphere results in 'quasi-merons' with non-half-integer numbers Q_S.

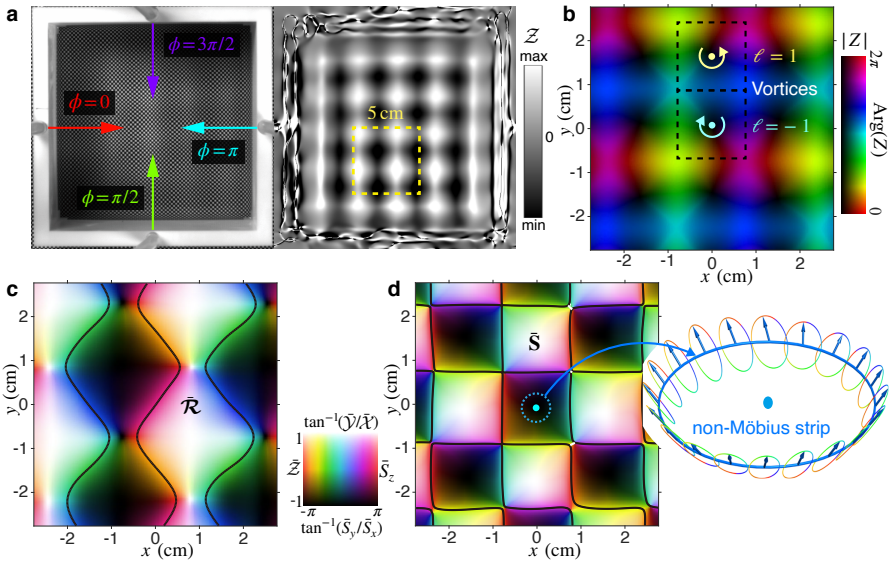

Extended Data Fig. 3 | Structures in the interference of four water waves. **a**, Same as in Fig. 2 but for the interference of four plane waves with the angles of propagation $\varphi = (0, \pi/2, \pi, 3\pi/2)$ and the corresponding phases delays $\phi = \varphi$. This field is equivalent (up to the global spatial shifts) to the interference of two orthogonal standing waves phase-shifted by $\pi/2$[28,34,35]. **b**, The complex vertical-displacement field $Z(x,y)$ exhibits a square lattice of $\ell = \pm 1$ vortices. **c**, The normalized 3D displacement field $\tilde{\mathcal{R}}(x, y, t = 0)$ does not contain skyrmions or merons (the black curves correspond to $\tilde{\mathcal{Z}}(x, y, t = 0) = 0$). **d**, The distribution of the normalized spin density $\mathbf{S}(x,y)$ exhibits 'quasi-merons', similar to the three-wave case in Extended Data Fig. 2. The black curves correspond to $S_z(x, y) = 0$. In contrast to the three-wave case, the polarization ellipses around centers of these quasi-merons do not form polarization Möbius strips. This because the C-points in the centers are double-degenerate due to the higher symmetry of the four-wave configuration.

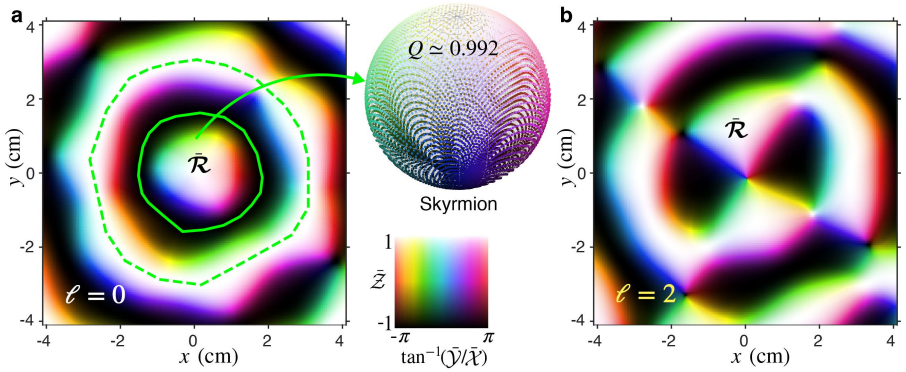

Extended Data Fig. 4 | Skyrmions in the Bessel modes. Distributions of the normalized instantaneous displacement vectors $\bar{\mathcal{R}}(x, y, t = 0)$ (encoded by the brightness and colors) in the generated Bessel modes with $\ell = 0$ and $\ell = 2$. **a**, The $\ell = 0$ non-vortex mode exhibits a skyrmion with $Q = 1$ in the center (the boundary is shown by the green solid curve). The topological charge integrated inside the dashed contour vanishes: $Q = 0$. **b**, Vortex Bessel modes with $\ell \neq 0$ (here $\ell = 2$) do not contain $\bar{\mathcal{R}}$-skyrmions.

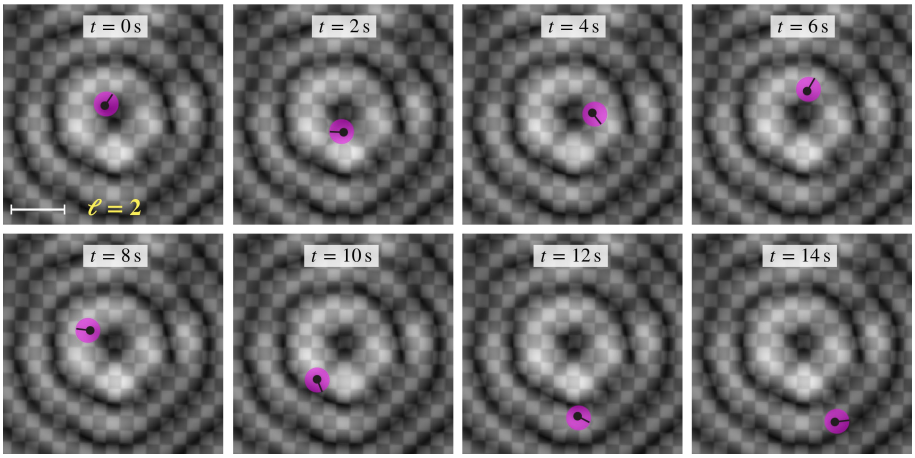

Extended Data Fig. 5 | Unstable trapping of floating particles. Dynamics of a floating particle with radius $a = 4.75$ mm in the Bessel-vortex wave with $\ell = 2$. Unlike Fig. 4c in the main text, here the particle is attracted to the intensity-maximum ring, orbits there for some time, and then escapes, because the radial centrifugal force prevails the trapping gradient force.

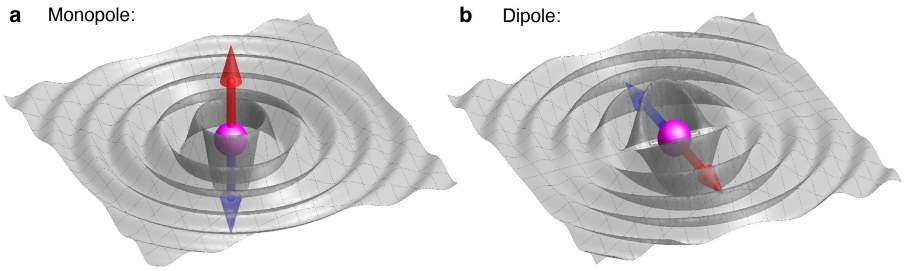

Extended Data Fig. 6 | Schematics of monopole-like and dipole-like water-wave excitations. a, Vertical oscillations of a small particle produce a monopole-like water-wave field. **b**, Horizontal oscillations of a small particle generate a dipole wavefield.